



The key role of metal dopants in nitrogen-doped carbon xerogel for oxygen reduction reaction

Sisi Liu ^{a, b}, Chengwei Deng ^{a, b}, Lan Yao ^{a, b}, Hexiang Zhong ^{a, *}, Huamin Zhang ^{a, **}

^a Division of Energy Storage, Dalian National Laboratory of Clean Energy, Dalian Institute of Chemical Physics, Chinese Academy of Sciences, Zhongshan Road 457, Dalian 116023, China

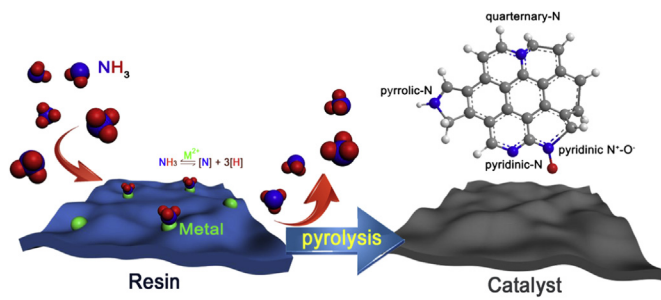
^b University of Chinese Academy of Sciences, Beijing 100039, China



HIGHLIGHTS

- The high active NCX catalyst was prepared by a simple sol–gel method.
- The effects of the metal on structure and activity were thoroughly investigated.
- Synthesis efficient between metal, N, C is crucial to achieve high ORR activity.
- The iron-based catalyst showed better activity than previous study.

GRAPHICAL ABSTRACT



ARTICLE INFO

Article history:

Received 27 April 2014

Received in revised form

14 June 2014

Accepted 26 June 2014

Available online 7 July 2014

Keywords:

Nitrogen doped xerogel

Metal effect

Non-noble metal catalyst

Fuel cell

ABSTRACT

Highly active non-precious metal catalysts based on nitrogen-doped carbon xerogel (NCX) for the oxygen reduction reaction (ORR) is prepared with resorcinol(R)-formaldehyde (F) resin as carbon precursor and NH_3 as nitrogen source. NCX samples doped with various transition metal species are investigated to elucidate the effect of transition metals on the structure and ORR activity of the products. As-prepared NCX catalysts with different metals are characterized using nitrogen-adsorption analysis, X-ray diffractometry, X-ray photoelectron spectroscopy, and Raman spectroscopy. The structural properties and ORR activities of the catalysts are altered by addition of different metals, and NCX doped with iron exhibits the best ORR activity. Metal doping evidently promotes the formation of more micropores and mesopores. Raman and XPS studies reveal that iron, cobalt, and nickel can increase pyridinic-N contents and that iron can catalyse the formation of graphene structures and enhance quaternary-N contents. Whereas the total N-content does not determine ORR activity, Metal-N₄/C-like species generated from the interaction of the metals with nitrogen and carbon atoms play important roles in achieving high ORR activity.

© 2014 Elsevier B.V. All rights reserved.

1. Introduction

Proton exchange membrane fuel cells (PEMFCs) are considered a promising technology for stationary and mobile applications because of their high energy conversion efficiency and power density, these devices promote the possibility of establishing a clean and sustainable society [1].

* Corresponding author. Tel.: +86 411 84379935.

** Corresponding author. Tel.: +86 411 84379072.

E-mail addresses: zhonghexiang@dicp.ac.cn (H. Zhong), zhanghm@dicp.ac.cn (H. Zhang).

But now, PEMFCs still have not world-wide commercialization. The high cost of PEMFCs remains a major barrier that hinders their application. Through the efforts during the past several years, the fuel cell cost has been reduced from \$ 275/KW in 2002 to \$61/KW in 2009. However, the 2015 United States Department of Energy's (DOE) targets for the fuel cell cost is \$30/KW so that to meet the demands of transportation applications [2]. The study to decrease the PEMFCs cost still has a long way to go.

The high cost of PEMFCs can partly be attributed to the membrane electrode assembly (MEA) that consists of a Nafion® membrane and catalyst layers [2,3]. State-of-the-art platinum/carbon (Pt/C) catalysts have been widely adopted as efficient cathode catalysts in catalyst layers for PEMFCs. However, the prohibitive cost and limited resource of Pt metal are the major drawback of this type of catalyst [4]. According to a DOE's report in 2007, the platinum-based catalyst layer comprises 56% of the total PEMFCs stack cost [5].

Hence, to realize the fuel cell final application, developing alternative non-platinum catalysts with high-performance and low-cost is necessary. Numerous efforts have been made to develop non-precious metal catalysts (NPMCs), such as metal nitrides [6,7], transition metal chalcogenides [8–10], metal-N₄ macrocycles [11–13], pyrolysed transition metal/nitrogen-containing complexes supported on various carbon materials [14–17] and doped carbon nanomaterial with heteroatoms [18–20]. Amongst these NPMCs, low-cost heteroatom-doped carbon materials with large surface areas and good electrical conductivity are some of the most advantageous materials in PEMFC applications.

The nitrogen atom, which has five valence electrons for bonding and an atomic size comparable with that of the carbon atom, has been widely used as a doping atom in carbon materials such as nitrogen-doped carbon nanotubes [21,22], nitrogen-doped graphene [23] and nitrogen-doped carbon nano fibers [24]. However, the nature of the active site of nitrogen-doped carbon catalysts remains controversial, especially in terms of the function of the transition metal in the catalyst. Some researchers believe that MeN_xC_y⁺ ions, such as Me–N₄/C and Me–N₂/C sites, are the main active sites for the ORR [14,25–28]. The measurement results of both extended X-ray absorption fine structure (EXAFS) and time of flight secondary ion mass spectrometry (ToF-SIMS) prove the existence of the MeN_xC_y⁺ structure [8,26,29].

Wu et al. [30] prepared a polyaniline-Me-C catalyst and confirmed the presence of the Me-Nx structure, which could enhance ORR activity, by X-ray photoelectron spectroscopy (XPS) and X-ray absorption fine structure spectra (XAFS). Qin et al. [31] assumed that Co-Nx and C–N sites respectively dominated the four- and two-electron transfer ORR processes. Li et al. [32] recently compared the ORR activity of iron containing carbon nanotube-graphene complexes in 10 mM KCN+0.1 M KOH electrolyte with that in 0.1 M KOH electrolyte. Upon attachment of the iron ion to CN[−] by coordinate bonds, the ORR activity of carbon nanotube-graphene complexes significantly decreased because the iron-centred catalytic site was inhibited by CN[−]. This phenomenon demonstrates that iron species have a significant function in promoting ORR activity.

Some articles suggest that doped metals of carbon catalysts are not a part of the catalytic active site [33–36]. The hypothesis in these studies claims that the transition metal only facilitates incorporation of nitrogen atoms into the carbon graphene matrix to form more active nitrogen–carbon structures with a high degree of edge exposure, thereby providing appropriate geometrical locations for nitrogen to incorporate into the carbon and finally form nitrogen groups, such as graphitic-N and pyridinic-N, as active sites [37,38].

Biddinger et al. [37] prepared several nanofibers with different edge plane exposure degrees. These edge plane exposures did not

improve ORR activity but provided appropriate geometrical locations for N incorporation. Maldonado et al. [24,39] constructed carbon nanofibers containing approximately 1% N through pyrolysis of iron(II) phthalocyanine on nickel substrates, demonstrating improved electro-catalytic activity for ORR. This enhanced activity was attributed to the presence of edge plane defects and nitrogen functional groups. Moreover, iron promoted stable incorporation of nitrogen into catalytic agents with a graphitic-like structure. Today, the identity and contribution of transition metals to catalytic activity remain incompletely understood.

Introduction of nitrogen atoms could significantly improve ORR activity because of the enhanced electron-donating ability and electron density resulting from the valence electrons donated by nitrogen [40]. Delocalization caused by nitrogen doping could also change the oxygen molecule adsorption mode from the end-on Pauling mode to the side-on Yeager mode on the catalyst surface. The parallel diatomic Yeager adsorption mode could effectively weaken O–O bonding, thereby facilitating the ORR process [20]. However, which nitrogen group has a more fundamental role in catalytic reactions is yet unknown.

Nitrogen in the nitrogen-doped carbon catalysts can be presented in different forms, including pyridinic-N, pyrrolic-N, quaternary-N and pyridine-N-oxide. Amongst these nitrogen groups, pyridinic-N and quaternary-N are believed to be correlated with ORR activity. Pyridinic-N possesses one lone pair of electrons along the plane of the carbon matrix, which can always be considered as the catalytic active centre [41,42]. Some researchers, however, have found that pyridinic-N is not an ideal candidate for the active centre because of the sluggish ORR activity observed in some catalysts with this type of nitrogen [43]. Quaternary-N, on the other hand, is both experimentally and theoretically considered an ORR catalytic site because of its reduced adsorption energy. Ni et al. [44] proved that graphite-like nitrogen more efficiently decreases the energy barrier than pyridine-like nitrogen using the density functional theory calculation method. Ikeda et al. [45] also confirmed that adjacent carbon atoms next to quaternary-N on zigzag graphene edges are active for ORR. Furthermore, quaternary-N is considered more stable than pyridinic-N in acidic media because of the lesser susceptibility of the former to protonation reactions [30,33].

In our previous work, we investigated the ORR activity and stability of nitrogen-doped carbon xerogel (NCX) [46,47]. Results showed that the catalyst presents high catalytic activity, superior stability and methanol tolerance in acidic and alkaline electrolytes. However, the role of the transition metal in promoting catalytic activity for the ORR remains unclear. An understanding of this relation is very important for effectively developing highly active non-precious catalyst. Therefore, in the present study, the effects of the metal on the ORR activity of catalysts doped with various metals were thoroughly investigated. Different catalysts with various transition metal species were prepared and characterized to study the effects of the metal species on catalyst structure and activity. The catalytic activities of post-treated and non-nitrogen doped catalysts for ORR were also studied to gain further insights into the nature of active sites.

2. Experimental

2.1. Catalyst preparation

NCX was prepared through the pyrolysis of metal-doped resorcinol (R)-formaldehyde (F) gels according to the method described in our previous work [46]: 6.16 g of R and 8.4 mL of F solution (37% F, aq.) were dissolved in 7 mL of deionised water and stirred for 2 h. Subsequently, 0.0028 mol of various metal salt [M:

$\text{FeSO}_4 \cdot 7\text{H}_2\text{O}$, $\text{Ni}(\text{NO}_3)_2 \cdot 6\text{H}_2\text{O}$, $\text{Co}(\text{NO}_3)_2 \cdot 7\text{H}_2\text{O}$, $\text{ZrO}(\text{NO}_3)_2$ and $\text{Ti}(\text{SO}_4)_2 \cdot 9\text{H}_2\text{O}$ (purchased from Damao Chemical Reagent Factory, Tianjin) solutions were slowly added. The initial pH of M was adjusted to pH 7–8 using 2 M ammonia solution. After stirring for 10 min to form uniform gels, polymerization of RF gels-M composites was initiated by addition of ammonia solution (28% NH_3 , aq.) until solidification. The obtained polymer was then cured at 60 °C in a vacuum oven for 7 d and powdered using a ball-mill with a rotating speed of 400 rpm. The resultant powder was pyrolysed at 800 °C for 2 h under an ammonia atmosphere flowing at a rate of 100 mL min⁻¹. The as-prepared NCX catalysts were denoted as M-NCX, where M represents the doped metal. A carbon xerogel without metal doping was also synthesised and used for comparison; this xerogel was denoted as NCX.

To study the effects of treatment conditions on catalytic activity, catalysts pyrolysed under nitrogen atmosphere (denoted as Fe-CX) and catalyst with post acid-treatment (denoted as Fe-NCX-W) were also investigated. The catalyst with post acid-treatment and post high temperature pyrolysis was denoted as Fe-NCX-WH. Fe-CX was prepared by a process similar to that described above. Subsequently, 1 g of prepared Fe-NCX catalyst was stirred into 100 mL of 2 M HNO_3 aqueous solution at 50 °C for 12 h to remove the metal species, followed by centrifugation, washing with DI water and drying process. After drying, Fe-NCX-W was further heated at 800 °C under a nitrogen atmosphere for 2 h to gain the resultant Fe-NCX-WH.

2.2. Electrochemical measurements

A CHI electrochemical station (Model 660B) equipped with a rotating disk electrode (RDE) system (EG&G Model 636) in a conventional three-electrode cell was used at room temperature for RDE measurements. A glassy carbon electrode (0.1256 cm²) was used as the working electrode. The rotating ring disk electrode (RRDE) measurement was performed using PINE Bipotentiostat model AFCBP1 electrochemical station. The working electrode was a rotating ring disk electrode with a glassy carbon disk (0.2475 cm²) and a ring made of platinum (0.1866 cm²). The RRDE collection efficiency is 0.37. The ring potential was set to 1.2 V to oxidize the hydrogen peroxide produced during oxygen reduction process on disk electrode.

A platinum plate (1 cm²) and a saturated calomel electrode were adopted as the counter electrode and reference electrode, respectively. The catalyst ink was prepared as follows: 5 mg of catalyst was ultrasonically dispersed in a solution containing 50 μL of 5 wt% Nafion® solution and 1 mL of isopropanol to form a homogeneous slurry. For RDE, 10 μL of the catalyst inks were dropped onto the glassy carbon electrode with a catalyst loading of 0.38 mg cm⁻² and dried at room temperature to obtain the working electrode. For RRDE, 20 μL of the catalyst inks were dropped onto the electrode to ensure the equal catalyst loading.

Cyclic voltammetry (CV) curves were obtained between –0.25 and 0.96 V at a scan rate of 50 mV s⁻¹ in N_2 -saturated 0.5 M H_2SO_4 . RDE and RRDE tests were conducted from 0.9 to –0.2 V at a scan rate of 5 mV s⁻¹ in O_2 -saturated 0.5 M H_2SO_4 with a rotating speed of 1600 rpm. The background current for all RDE measurements was corrected. All the potentials were measured using a standard hydrogen electrode (SHE) as reference.

2.3. Physical and chemical characterization

Using a DX-2700 (Dandong Haoyuan Instrument Co., Ltd., China) diffractometer with $\text{Cu K}\alpha$ radiation ($\lambda = 0.1541$ nm) operated at 40 kV and 40 mA, X-ray diffractometry (XRD) patterns were obtained to investigate the structures of the catalysts.

X-ray photoelectron spectroscopy (XPS) was used to determine the surface composition and nitrogen species of the catalysts. XPS characterization was performed using a VG ESCALAB250 spectrometer with $\text{Al K}\alpha$ radiation. All of the spectra were calibrated according to the C1s (284.6 eV) peak. The spectra were analysed using XPS Peak 4.1 with a Gaussian–Lorentzian mix function (Gaussian to Lorentzian ratio: 30:70) and Shirley background subtraction.

The surface area and pore texture of the catalysts were determined on a QuadraSorb SI automated surface area and pore size analyser at –196 °C. Surface areas were estimated using the Brunauer–Emmet–Teller (BET) equation. Before testing, the samples were treated at 350 °C for 4 h to remove impurities.

Raman spectra measurements were performed on a Renishaw Raman microscope at room temperature. The excitation source was operated at 514 nm. The Raman data were analysed using Peakfit 4.12 software.

3. Results and discussion

3.1. Electroactivity characterization

CV and linear sweep voltammogram (LSV) curves of the various metal-doped carbon xerogels are shown in Fig. 1.

Fig. 1(a) demonstrates that the CV curves of all of the metal-doped NCX except Fe-NCX present no obvious peaks. Instead, a quasi-rectangular shape, which is typical of a high-surface-area carbon material was observed.

The CV curve of Fe-NCX displays a pair of well-developed redox peaks at about 0.635 V. The absolute values of the anodic and cathodic peak currents are nearly equal. The distance potential of the two peaks is within 59 mV, and the peak areas are similar. These characteristics suggest that the corresponding redox process should be expected for a reversible electrochemical reaction of $\text{Fe}^{2+}/\text{Fe}^{3+}$ [48,49].

The LSV curves of the various metal-doped carbon xerogels were obtained to evaluate the function of metal species in ORR activity. Fig. 1(b) clearly shows that ORR activity is greatly affected by the metal type. Fe-NCX exhibits the best activity, with an ORR onset potential of 0.823 V and half-wave potential of 0.697 V, followed by Co-NCX, with an ORR onset potential of 0.772 V and half-wave potential of 0.689 V. Compare this result with other latest reported Fe–N catalysts [50,51], Fe-NCX displays higher onset potential and half-wave potential, along with increase diffusion-limited current density, which indicates to the high amount and uniform distribution of ORR active sites on the catalyst surface [50].

The ORR activity of NCX without metal doping is much lower than those of Fe-NCX, Co-NCX. This result demonstrates that metal has an important function in improving the ORR activity of M-NCX, which is consistent with findings in other studies [52,53]. Overall, Fe-NCX showed the best activity.

3.2. Physicochemical characterisation

Fig. 2 shows the nitrogen adsorption–desorption isotherms of the various metal-doped carbon xerogels. The physical properties of these xerogels are listed in Table 1.

The metal dopant has an evidently profound effect on the nanostructure of the resulting carbon xerogel catalyst. All of the samples exhibit a type IV adsorption isotherm, which is characteristic of microporous/mesoporous materials. The hysteresis loop can provide important information on the pore structure of catalysts. Fig. 2 clearly shows that the hysteresis loops slightly differ amongst the different catalysts studied. Most of the catalysts exhibit an H4 hysteresis loop, which is associated with narrow slit-

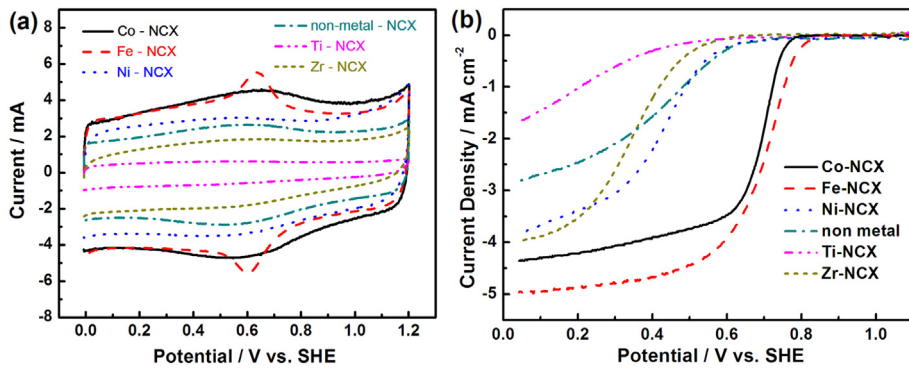


Fig. 1. (a) Cyclic voltammograms of M-NCX catalysts in N₂-purged 0.5 M H₂SO₄ solution. Scan rate: 50 mV s⁻¹. (b) Linear sweep voltammograms of M-NCX catalysts in O₂-purged 0.5 M H₂SO₄ solution. Scan rate: 5 mV s⁻¹. Rotation rate: 1600 rpm.

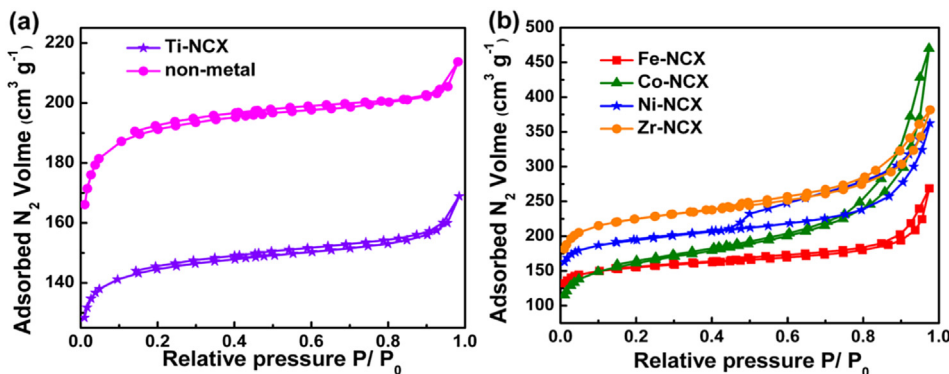


Fig. 2. N₂ sorption isotherms of various metal-doped carbon xerogels: (a) Ti-NCX and the non-metal catalyst and (b) Fe-NCX, Co-NCX, Ni-NCX and Zr-NCX.

like pores. However, Ni-NCX exhibits an H2 hysteresis loop, which are often referred to as 'ink bottle' pores [54].

In all of the samples, the increase in absorbed gas volume at relatively low pressure is characteristic of the presence of microspores; by contrast, the hysteresis loop represents mesoporous features [55]. These results indicate that the as-prepared carbon materials contain both micropores and mesopores. Compared with NCX without metal dopant, Fig. 2(b) reveals that the hysteresis loops of the catalysts doped with various transition metals (except Ti) become larger and shift toward higher P/P₀ values, which indicates increments in mesopore size and pore volume [55]. Ti metal can promote the formation of micropores, which results in a decrease in pore volume.

The BET data demonstrate that all of the samples show large surface and microporous areas. This phenomenon can be explained in three aspects: (1) the original 3D morphology of the porous RF resin precursor; (2) the micropores and mesopores formed from

the collapse of macropores under high temperature, which increase the material surface area; and (3) the etching process in which ammonia directly reacts with the carbon material, resulting in micropore formation and larger surface areas. Thus, the NCX catalysts have a large BET surface area of 763 m² g⁻¹.

Compared with NCX, all of the metal-doped catalysts (except Zr-NCX) show low BET surface areas. This result may be attributed to the formation of surface impurities, such as metal oxides or metal nitrides, as confirmed by the XRD patterns obtained. Zr salts have been previously reported to promote pore-structure formation; as such, Zr-NCX may be expected to have a large surface area [56].

From the BET results, we can conclude that different metals have different impacts on the catalyst structure and that no direct connection in this study was observed between the structure parameters and ORR activity.

Results of our structural and phase analyses of the various metal-doped catalysts are confirmed by the XRD patterns shown in Fig. 3.

Regardless of the type of metal used for doping, all of the catalysts clearly exhibit broad diffraction peaks located at ca. 24.5°, which is attributed to (002) basal plane diffraction along the graphitic structure. NCX shows only one obvious peak at ca. 43.2°, which may be assigned to the (100) plane of graphitic C. The peak of Me-NCX at 43.2° is overshadowed by the peaks of other by-products. The XRD results indicate that the carbon xerogel without metal dopant presents a disordered amorphous structure because of the original 3D-network structure of the RF resin and the relatively low pyrolysis temperature.

The Co-NCX catalyst exhibits the characteristics of a cubic crystalline structure carbon nitride (Co_{5.47}N), with (111) and (200) diffraction peaks observed at ca. 43.3° and 50.7° (PDF Card No.: 00-

Table 1

Physical properties of the metal-doped carbon xerogels.

Sample	BET surface area (m ² g ⁻¹) ^a	Pore volume (cm ³ g ⁻¹) ^b	Micropore area (m ² g ⁻¹) ^c	External surface area (m ² g ⁻¹) ^c
Non metal	762.918	0.3306	710.281	52.636
Fe-NCX	607.712	0.4159	519.466	88.264
Co-NCX	595.704	0.7266	374.627	221.867
Ni-NCX	757.304	0.5609	619.404	137.901
Ti-NCX	576.244	0.2612	534.648	41.596
Zr-NCX	869.203	0.5906	708.011	161.192

^a BET was obtained in the range of 0.01–0.05 P/P₀.

^b Total pore volumes were calculated as the amount of N₂ adsorbed at a relative pressure of 0.974.

^c The area was calculated using the t-method.

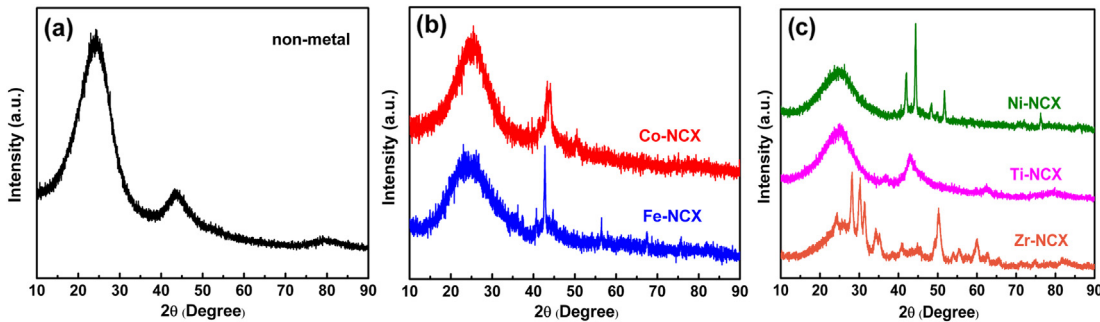


Fig. 3. XRD patterns of (a) the non-metal catalyst, (b) Co-NCX and Fe-NCX and (c) Ni-NCX, Ti-NCX and Zr-NCX.

041-0943), respectively, and a small amount of metallic cobalt, with a (111) peak diffraction at ca. 44.2° (PDF Card No.: 00-015-0806). The main peaks of the Fe-NCX catalyst are ascribed to iron nitride with (002) and (011) diffraction signals at ca. 40.8° and 42.9° (PDF Card No.: 01-072-2126), respectively. The obtained XRD patterns indicate that in high active Co-NCX and Fe-NCX, metal nitride is the dominant metal species.

In the Ni-NCX catalyst, the main peaks at ca. 44.4°, 51.6° and 76.2° are respectively assigned to the (111), (200) and (220) planes of metallic nickel (PDF Card No.: 00-001-1258). A small amount of nickel nitride (Ni_4N) can also be observed at ca. 41.8°, which is attributed to the (111) plane. The XRD pattern of Ti-NCX contains peaks at 36.8°, 43.1° and 62.5°, which may be respectively assigned to the (111), (200) and (220) planes of titanium oxide [($\text{TiO}_{0.716}$)_{3.76}; PDF Card No.: 01-073-1774]. The XRD pattern of Zr-NCX shows a complex of different zirconium oxides. The main peaks at ca. 30.2°, 50.4°, and 60.1° are respectively attributed to the (101), (112) and (211) planes of tetragonal zirconium oxide (PDF Card No.: 01-080-2155). Moreover, the peaks at ca. 28.1° and 31° can be respectively assigned to the (-111) and (111) planes of monoclinic zirconium oxide (PDF Card No.: 01-001-0750).

Combining the data above, iron and cobalt are evidently suitable for forming metal-nitride compounds, whereas other metals tend to form metal oxides. Iron and cobalt can coordinate with nitrogen to form metal/nitrogen complexes. Whether the metal-nitride compound or the metal/nitrogen species is responsible for ORR activity in the catalysts is discussed in the following section.

To characterize the crystal structure of the catalysts, particularly their crystal defects and ordered and disordered structures, Raman spectroscopy was used to characterise the various metal-doped carbon xerogel catalysts (Fig. 4).

As shown in Fig. 4, after deconvolution, the spectrum of each catalyst fits into a series of peak sand is dominated by two peaks at about 1355 and 1590 cm^{-1} , which can be assigned to the G and D bands, respectively, of a typical carbon material. The G band arises from the E_{2g} vibrational D_{6h}^4 symmetry group in an ideal graphene layer, which indicates the presence of crystalline graphitic carbon. The origin of the D band is unclear, but it is generally accepted to arise from a Raman inactive mode (A_{1g}), which becomes active by the reduction in symmetry at or near crystalline edges [57]. The D band corresponds to a disordered structure. Besides these two main bands, two broad peaks at ca. 1220 and 1510 cm^{-1} are also observed on the overall Raman spectrum of each catalyst; these peaks are denoted as the I and D_1 bands, respectively, and are attributed to a relaxation in symmetry from a perfectly planar graphene sp^2 network lattice distortion, which is associated with amorphous carbon or heteroatoms in a graphene structure [30,39,58].

Details of the Raman spectra are listed in Table 2.

Direct measurements of distinct FWHM yield imprecise results because of the large overlap between the D and G bands [39]. However, all of the catalysts evidently have broad D and G bands

and high area ratios, which suggest that the catalysts are typical porous carbons with a high degree of structural disorder, consistent with the XRD patterns obtained.

The influence of the doping metal on the carbon crystalline structure is shown in Fig. 4 and Table 2. The intensity ratio of the two bands (I_D/I_G) is considered a key parameter in evaluating the degree of disorder of the carbon material. Clearly, compared with the non-metal doped catalyst, the metal-doped catalysts (except Fe-NCX) exhibit higher I_D/I_G , which indicates a higher degree of disorder or defects. Amongst these catalysts, Co-NCX has the highest I_D/I_G . The XPS data show that Co-NCX also has a much larger amount of pyridinic-N, which indicates surface disorder and defects. Interestingly, Fe-NCX is highly active but its I_D/I_G ratio is the lowest amongst the samples. Raman results and findings in a related study [30] indicate that iron can also catalyse the formation of graphite-like carbon structures or graphite pieces. Considering the correlation between the graphite-structure and the 'in-plane $\text{Fe}-\text{N}_4$ centre (considered an active centre), the high activity of Fe-NCX may be reasonably explained. However, further analysis is necessary before accurate conclusions may be made.

XPS measurement was performed to gain better insights into the effect of metal type on the nanostructure and surface species of the catalysts and elucidate the relationship between catalyst structure and catalyst activity.

The N1s region of the XPS patterns of both catalysts can be deconvoluted into four peaks (Fig. 5) attributed to four different nitrogen-containing groups, i.e., pyridinic-N (398.3 eV \pm 0.2 eV, N1), pyrrolic-N (400.2 eV \pm 0.2 eV, N2), quaternary-N (401.3 eV \pm 0.2 eV, N3) and pyridine-N-oxide (403.5 eV \pm 0.2 eV, N4) [22,30,40,53]. Pyridinic-N is always located along the edge of graphite planes, bonds with two carbon atoms, and donates one p electron to the aromatic π system to impart Lewis basicity to the carbon. According to the literature [59], pyridinic-N is capable of adsorbing molecular oxygen and intermediates and facilitates the reductive adsorption of O_2 . Pyrrolic-N refers to the N atoms incorporated into five-membered heterocyclic rings; this type of nitrogen bonds with two carbon atoms and contributes two p electrons to the π system. Quaternary-N can also be described as 'graphitic nitrogen', wherein nitrogen atoms are inserted into a perfect graphite plane and bonded with three carbon atoms. Pyridine-N-oxide refers to the N atom bonded with two carbon atoms and one oxygen atom, which formed by the reaction of oxygen with the carbon material [40]. Pyridine-N and pyrrolic-N are always located along the edge of the graphite plane and are considered as 'edge-N'. Quaternary-N can insert into the carbon matrix and may be found on the edge, i.e., it can act as both 'bulk-N' and 'edge-N'. The locations of different N groups described above are illustrated in Fig. 6.

The surface compositions of different catalysts are listed in Table 3. Results show that the transition metal can significantly affect the total nitrogen concentration of the catalysts.

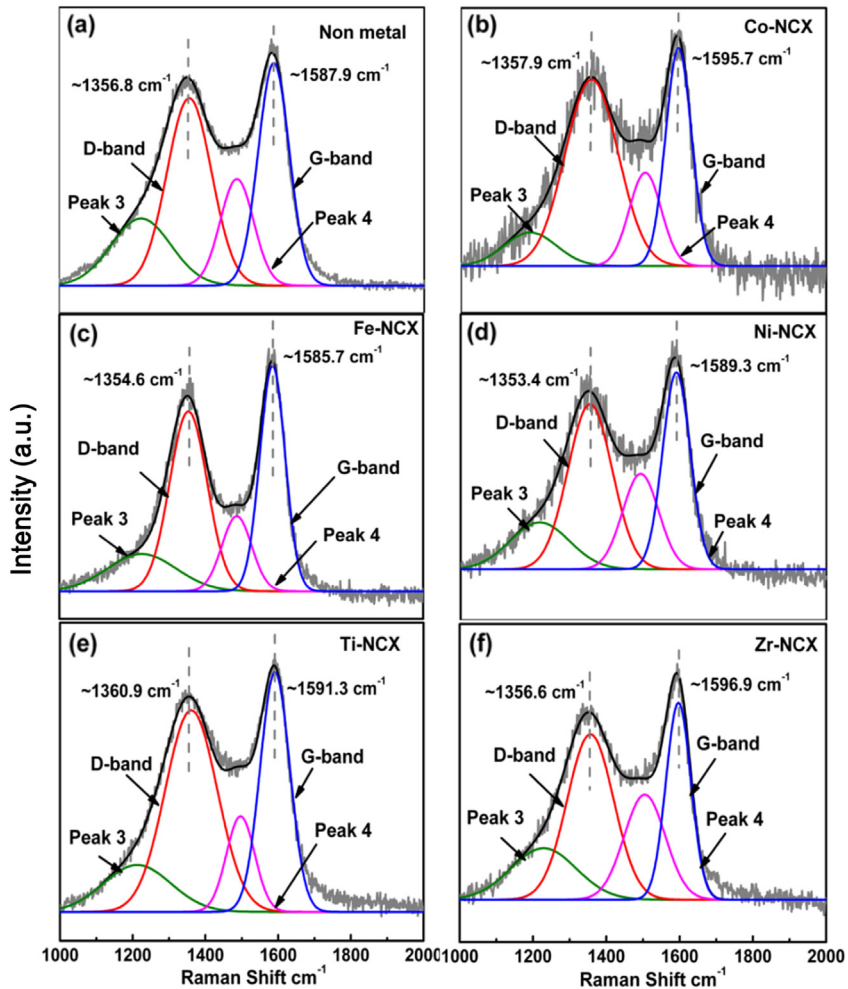


Fig. 4. Raman spectra of (a) the non-metal catalyst, (b) Co-NCX, (c) Fe-NCX, (d) Ni-NCX, (e) Ti-NCX and (f) Zr-NCX.

Clear catalytic activity from the LSV test, which shows no direct correlation with the nitrogen concentration, is observed. Ti-NCX has the highest nitrogen concentration but exhibits the worst activity amongst the catalysts. The non-metal doped NCX also exhibits a high nitrogen concentration, which shows lower activity. It demonstrates that the catalytic activity of the M-NCX shows no direct correlation with the nitrogen concentration.

The N1s configurations of the different catalysts significantly vary, as observed in the detailed deconvolution of the N1s spectra (Fig. 5). The relative composition ratios of N in the various metal-doped catalysts are summarized in Table 4.

Using similar FWHMs and 30% of the Lorentzian–Gaussian function to optimise peak assignment, the deconvolution peaks of each catalyst feature close binding energies of ± 0.2 eV. Moreover,

each catalyst forms a peak at about 400.5–400.7 eV because of the proximate binding energies of pyrrolic and quaternary nitrogen groups. The pyridinic nitrogen to pyrrolic + quaternary nitrogen ratio also increases with the amount of doped metal, which demonstrates that the metal can promote edge-N formation.

Table 4 shows that the highly active Fe-NCX and Co-NCX catalysts have elevated $N1/(N2+N3)$ ratios and display higher pyridinic-N contents than the other catalysts, resulting in a higher proportion of edge plane exposure. This result is consistent with the BET findings. Compared with the non-metal doped catalysts, Fe-NCX and Co-NCX have larger pore volumes and form more microspores and mesopores, which may provide favourable sites and plane edges for both the pyridinic-N and a small amount of quaternary-N. Jaouen et al. [60] suggested that the active sites are hosted in microspores. It suggests the addition of Fe and Co may promote the formation of the active sites in the micropores.

The pyridinic-N with lone pair electrons is always considered the ORR active site. However, comparing the gross pyridinic-N contents of both Fe-NCX and Co-NCX, the Fe-NCX catalyst with higher activity has lower pyridinic-N. Moreover, Fe-NCX has relatively higher quaternary-N contents. Combined with the Raman results, it revealed that iron promotes interior doping of nitrogen atoms into the graphene layer, thereby forming a larger number of intrinsically active ORR sites to increase ORR activity. Similar findings have been obtained by Wu et al. [61,62]. Nevertheless, the non-metal doped catalyst has similar gross nitrogen contents, nitrogen

Table 2

Summary of the Raman spectra of the various metal-doped carbon xerogels.

Sample	I_D/I_G (intensity)	D band Position (cm^{-1})	G band Position (cm^{-1})
Non metal	0.842	1356.8	1587.9
Fe-NCX	0.797	1354.6	1585.7
Co-NCX	0.857	1357.9	1595.7
Ni-NCX	0.838	1353.4	1589.3
Ti-NCX	0.841	1360.9	1591.3
Zr-NCX	0.839	1356.6	1596.9

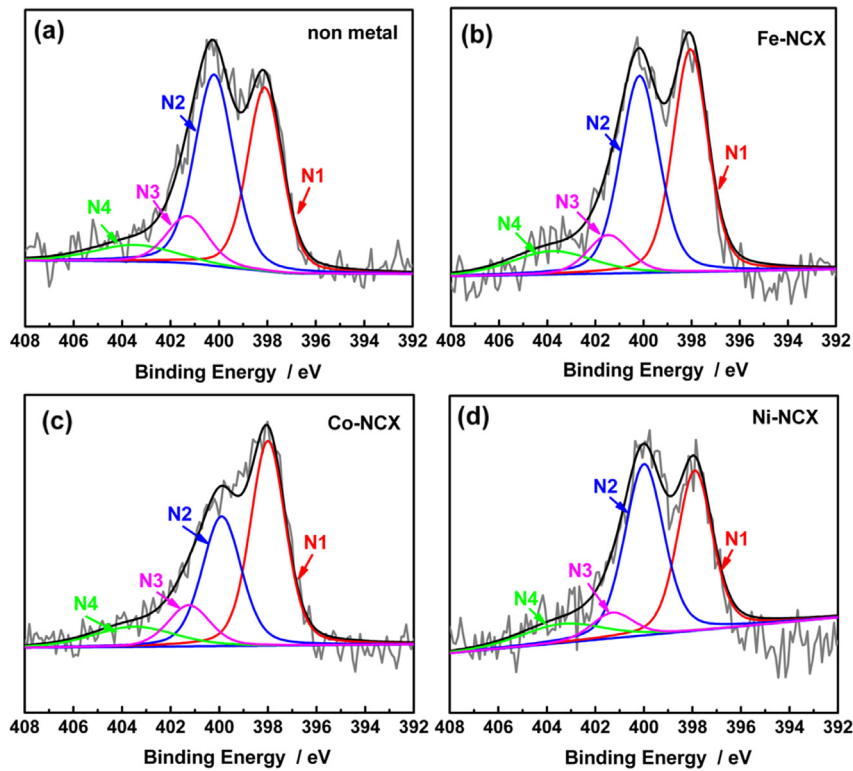


Fig. 5. XPS spectra of the deconvoluted N1s region of (a) the non-metal doped catalyst, (b) Fe-NCX, (c) Co-NCX, and (d) Ni-NCX.

groups, and relative nitrogen contents to those of Fe-NCX, although its ORR activity is relatively low. Therefore, the metal is proved to play an important role in ORR activity. Based on the XPS data and previous study, metal/nitrogen coordinate ORR active sites such as FeN_4/C -like species [63] are deemed to probably be the ORR active site that can weaken oxygen adsorption energy to enhance ORR activity.

3.3. Effect of acid leaching

To investigate the possible role of metal species further, Fe-NCX-W and Fe-NCX-WH were synthesized through acid leaching and secondary heat-treatment. Fig. 7(a) shows RDE measurements obtained to assess the impact of acid leaching and secondary heat-treatment on the ORR activity of the resultant catalysts.

Prior to acid treatment, the activity of Fe-NCX is high. However, after acid leaching, both the half-wave potential and limiting current density of the catalyst significantly decrease. After nitric acid

treatment, the catalyst is partly oxidised and various oxidation groups can be found on the catalyst surface, as confirmed by XPS. These oxides may cover the original ORR active sites hosted in mesopores or micropores, resulting in decreased activity.

After a second heating treatment in a nitrogen atmosphere, a slightly positive shift in onset potential as well as a decrease in the mass limiting current density may be observed. The onset ORR potential of each catalyst does not obviously change during acid leaching or heat treatment, which suggests that the original type of ORR site in the catalyst has not changed [43].

After heat treatment, oxidation groups on the catalyst surface are decomposed, which exposes the active sites previously covered by these groups. The acid leaching process also removes unstable impurities [Fig. 7(b)] such as iron nitrides, exposing more active sites previously covered by these impurities and ultimately resulting in markedly higher ORR activity in Fe-NCX-WH. It is obvious that iron-nitride does play a key role in the ORR activity. However, after acid washing, XPS results reveal that trace iron remains in the sample (0.1 at.%). Trace iron reportedly contributes to high-activity synergistic effects between doped-N and -Fe atoms [64].

The deconvoluted N1s spectra of Fe-NCX-W and Fe-NCX-WH are shown in Fig. 8.

The N5 peak of Fe-NCX-W at around 405.5 eV can be assigned to chemisorbed nitrogen oxide species formed by nitric acid leaching. In Fe-NCX-WH, the disappearance of this peak suggests that the species decomposes under high temperature.

Details of the relative composition ratios of the N groups in the three catalysts are summarized in Table 5.

The pyridinic-N content decreases after acid leaching because of its instability in acidic media. Pyrrolic-N and quaternary-N are more stable than pyridinic-N. The function of different nitrogen groups in ORR activity, particularly those of pyridinic-N and quaternary-N, remain debatable. Biddinger et al. [37] proposed that pyridinic-N promotes ORR activity, and Lai et al. [40] found that the presence of pyridinic-N can improve the onset potential of the

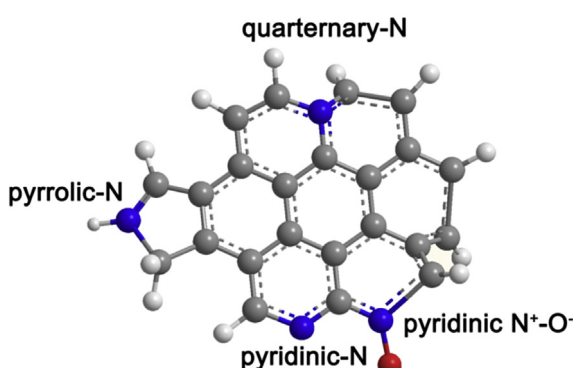


Fig. 6. Schematic diagram of different N groups incorporated into the carbon matrix.

Table 3

Surface compositions of the various metal-doped catalysts derived from the XPS spectra (atom ratio %).

Sample	C%	O%	N%	Metal%
Non metal	84.22	14.44	1.33	0.00
Fe-NCX	83.59	15.19	1.16	0.07
Co-NCX	82.41	16.30	1.18	0.11
Ni-NCX	83.14	19.59	0.80	0.10
Zr-NCX	82.30	16.94	0.70	0.06
Ti-NCX	81.88	13.28	3.30	1.54

Table 4

Concentrations of N-containing groups present in the various metal-doped catalysts (relative ratio %).

Sample	N1	N2+N3	N4	N1/(N2+N3)
Non metal	37.15	54.79	8.06	0.678
Fe-NCX	40.95	48.94	10.11	0.837
Co-NCX	45.84	43.46	10.70	1.055
Ni-NCX	37.49	51.98	10.53	0.721

resultant catalyst. In this article, the pyridinic-N content in Fe-NCX-WH is less than that in Fe-NCX and the onset potential of Fe-NCX-WH is slightly more positive than that of Fe-NCX. However, the limiting current density of the former is lower than that of the latter. Hence, we propose that the limiting current density depends on the pyridinic-N content.

Quaternary-N has recently been experimentally [65] and theoretically [66] proposed as an ORR active site because of its reduced adsorption energy. In the present study, establishing a clear relationship between independent quaternary-N content and catalytic performance is difficult. Thus, combine with XPS and LSV results, we propose that the metal/nitrogen complex fragment, which was previously detected by Mössbauer spectroscopy [67] in another study, is an important promoter of ORR activity.

From the XPS data of the catalysts, we conclude that: (1) no connection exists between gross N content and ORR activity; (2) the specific nitrogen is combined with iron species, forming Fe/N/C fragments that are important for ORR activity; and (3) the metal is a necessary factor in improving ORR activity.

3.4. Effect of ammonia treatment

Heat treatment under an ammonia atmosphere is known to incorporate nitrogen into the carbon matrix. We pyrolysed the precursor at 800 °C under a nitrogen atmosphere, denoted the resulting catalyst Fe-CX and compared it with Fe-NCX.

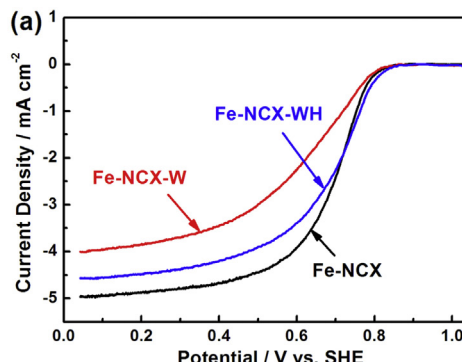


Fig. 7. (a) Polarization curves of Fe-NCX, Fe-NCX-W and Fe-NCX-WH in 0.5 M H₂SO₄ saturated with O₂ and (b) XRD patterns of Fe-NCX, Fe-NCX-W and Fe-NCX-WH.

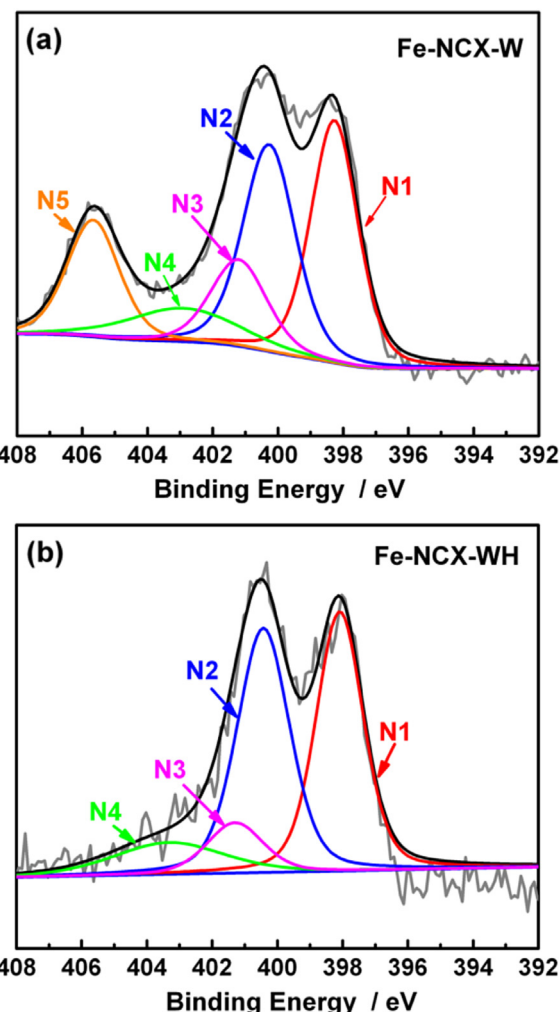


Fig. 8. XPS spectra of the deconvoluted N1s region of (a) Fe-NCX-W and (b) Fe-NCX-WH.

As shown in Fig. 9, the ORR activity of Fe-CX is very low. The main components of Fe-CX are iron oxide and iron; in this catalyst, the nitrogen content may easily be neglected. Ammonia treatment seems to directly dope nitrogen into the carbon. Ammonia has been proposed to introduce nitrogen into the carbon matrix through a complex corrosion process, during which ammonia reacts with the catalyst to form HCN or H₂ to yield the successful incorporation of nitrogen into carbon [35,37]. Iron can promote this process and be incorporated with nitrogen and carbon to form active sites.

Table 5

Concentrations of N-containing groups present in Fe-NCX before and after post-treatment (relative ratio %).

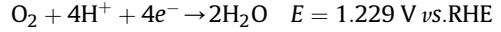
Sample	N1	N2+N3	N4	N5	N1/(N2+N3)
Fe-NCX	40.95	48.94	10.11	0	0.837
Fe-NCX-W	30.88	42.62	9.99	16.49	0.724
Fe-NCX-WH	39.18	49.50	11.3	0	0.792

3.5. Kinetic parameters

Finally, we investigated the kinetic parameters of Fe-NCX and Co-NCX. ORR can occur in acidic conditions through two possible

pathways: through the direct four-electron pathway, wherein the original molecular oxygen is reduced to form H_2O , and through the two-electron pathway, wherein the molecular oxygen is reduced to the intermediate production of hydrogen peroxide and further reduced to form H_2O [49]. These two pathways are listed below:

Four-electron pathway:



Two-electron pathway:

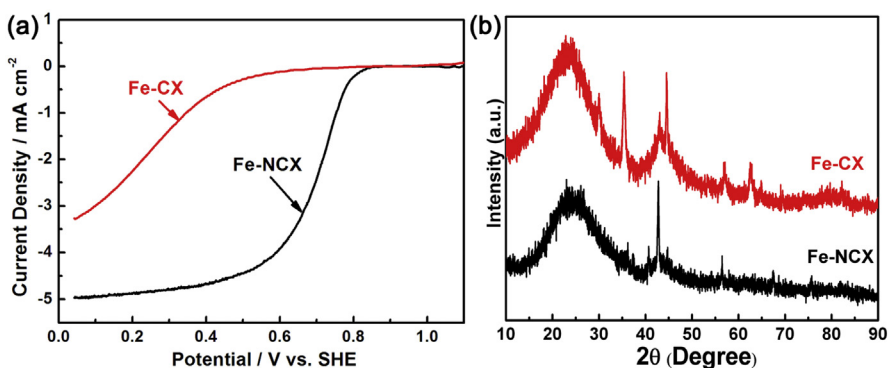
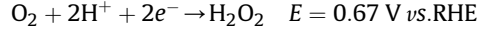


Fig. 9. (a) Polarization curves of Fe-NCX, Fe-CX in 0.5 M H_2SO_4 saturated with O_2 and (b) XRD patterns of Fe-NCX and Fe-CX.

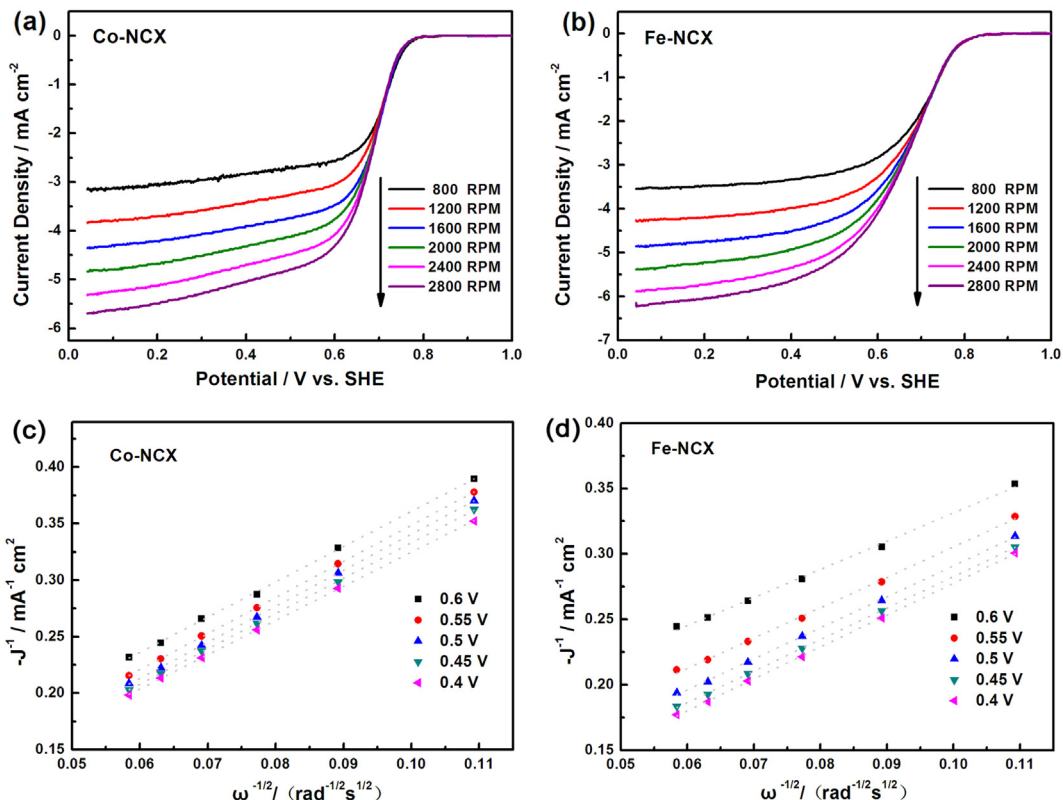
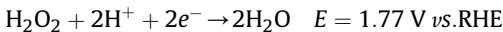


Fig. 10. Polarization curves of (a) Co-NCX and (b) Fe-NCX at various rotating rates in 0.5 M H_2SO_4 saturated with O_2 and Koutecky–Levich plots recorded at selected potentials of (c) Co-NCX and (d) Fe-NCX.



Higher ORR transfer electron-numbers indicate that the catalyst is more active and efficient. The ORR transfer electron number of the NCX catalysts is calculated using the first-order Koutecky–Levich (K–L) equation under different potentials,

$$\frac{1}{J} = -\frac{1}{J_k} + \frac{1}{0.62nFD^{2/3}cv^{-1/6}\omega^{1/2}} \quad (1)$$

where J is the measured current density, J_k is the kinetic current density, n is the number of electrons transferred, F is the Faraday constant ($96,485 \text{ C mol}^{-1}$), D is the diffusion co-efficiency of O_2 in $0.5 \text{ M H}_2\text{SO}_4$ ($1.93 \times 10^{-5} \text{ cm}^2 \text{ s}^{-1}$), c is the bulk concentration of dissolved O_2 in the electrolyte ($1.13 \times 10^{-6} \text{ mol L}^{-1}$), v is the kinematic viscosity of $0.5 \text{ M H}_2\text{SO}_4$ ($0.0095 \text{ cm}^2 \text{ s}^{-1}$) and ω is the rotation rate (rad s^{-1}). According to Eq. (1), the slope of the J^{-1} versus $\omega^{-1/2}$ plot can estimate the electron transfer number (n). Fig. 10 shows the K–L plots of Co-NCX and Fe-NCX at different rotation speeds and potentials.

The transfer electron numbers calculated from Fig. 10(b) and (d) are 3.49 and 3.82 at 0.5 V for Co-NCX and Fe-NCX, respectively. These values indicate that ORR proceeds by domination of the four-electron pathway and that most O_2 molecules are directly reduced to H_2O . This demonstrates the high selectivity of the ORR on the NCX catalysts.

Besides, we can also calculate the kinetic current density as follows:

$$\frac{1}{J_k} = \frac{J \times J_{\text{lim}}}{J - J_{\text{lim}}} \quad (2)$$

Where J is the measured current density, J_k is the kinetic current density, J_{lim} is the limiting diffusion current density. The kinetic

current density of the different catalysts at various potentials is tabulated in Table 6. Higher current density is observed in the Fe-NCX catalyst, which indicates higher catalyst active site density.

To further gain insight into the mechanism, RRDE measurement was performed. The hydrogen peroxide yield ($\% \text{H}_2\text{O}_2$) in the ORR and the total electron transfer number (n) is calculated as follows, the detail results are shown in Fig. 11.:

$$\% \text{H}_2\text{O}_2 = \frac{2I_r}{N|I_d| + I_r} 100\% \quad (3)$$

$$n = 4 - 2 \times \frac{\% \text{H}_2\text{O}_2}{100} \quad (4)$$

Where I_d is disk current, I_r is ring current, N is the RRDE collection efficiency (0.37). On the basis of the ring and disk currents, the electron transfer number (n) for Co-NCX is calculated to be 3.45–3.79 over the potential range from 0.2 to 0.7 V . For Fe-NCX, the value is calculated to be 3.78–3.91. Moreover, the H_2O_2 yield for Fe-NCX (4.3–10.8%) is obviously lower than Co-NCX catalyst (11.2–27.4%), This further proves the Fe-NCX exhibits better selectivity than Co-NCX. This is consistent with the K–L results.

4. Conclusion

NCX was prepared by an easy method followed by subsequent pyrolysis under ammonia atmosphere. Various metal salts were used as metal precursors to elucidate the effect of the metal on the ORR activity and structure of NCX. The results demonstrate that the metal has a great impact on both the ORR activity and physical properties of the resultant catalyst, and the catalyst doped with iron showed excellent ORR activity (0.823 V vs. SHE onset potential). The doped metals could also significantly affect the pore structure of the catalysts. Compared with NCX, M-NCXs presented more micropores and mesopores, which may contribute their higher activity. Iron, cobalt and nickel increased the pyridinic-N contents and edge exposures of the resultant catalysts. The presence of Fe species during carbonisation contributed to the growth of the graphene structure and enhanced the quaternary-N contents of the catalysts, which may improve the activity of the NCX catalyst. No direct correlation was observed between gross nitrogen contents and catalytic activity, but the metal species incorporated with nitrogen plays an important role in promoting ORR activity.

Table 6
Kinetic current densities of different catalysts at various potentials.

Kinetic current density J_k (mA cm^{-2})		
	Co-NCX	Fe-NCX
0.7 V	3.095	3.257
0.72 V	1.453	2.149
0.75 V	0.327	0.973

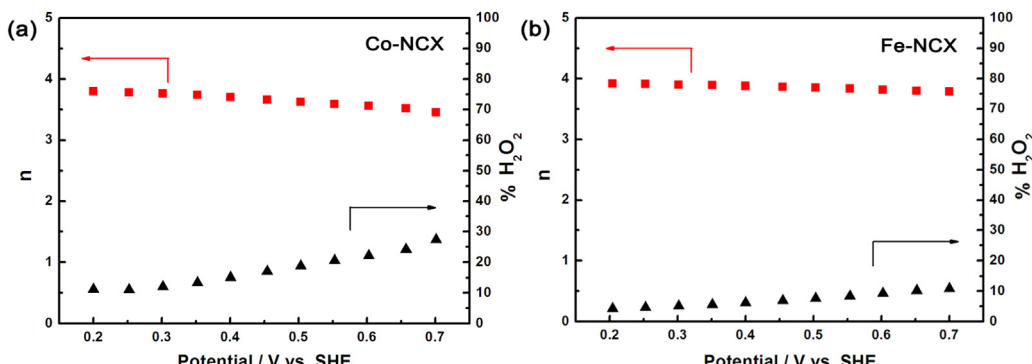


Fig. 11. Electron transfer number (n) and $\% \text{H}_2\text{O}_2$ of (a) Co-NCX (b) Fe-NCX catalysts, obtained at 1600 rpm.

Acknowledgements

Financially support for this research was provided by DNL-Topsøe Scholarship, National Program on Key Basic Research Project (973 Program, No. 2012CB215500) and the National Natural Science Foundation of China (No. 21006103). The author also appreciates Dr. Yan Lv for his help with relevant art work.

References

- [1] Y. Nabee, S. Moriya, K. Matsubayashi, S.M. Lyth, M. Malon, L. Wu, N.M. Islam, Y. Koshigoe, S. Kuroki, M.-a. Kakimoto, *Carbon* 48 (2010) 2613–2624.
- [2] Y. Wang, K.S. Chen, J. Mishler, S.C. Cho, X.C. Adroher, *Appl. Energy* 88 (2011) 981–1007.
- [3] E. Fabbri, D. Pergolesi, E. Traversa, *Chem. Soc. Rev.* 39 (2010) 4355–4369.
- [4] Y. Zheng, Y. Jiao, J. Chen, J. Liu, J. Liang, A. Du, W. Zhang, Z. Zhu, S.C. Smith, M. Jaroniec, *J. Am. Chem. Soc.* 133 (2011) 20116–20119.
- [5] Z. Chen, D. Higgins, A. Yu, L. Zhang, J. Zhang, *Energy Environ. Sci.* 4 (2011) 3167–3192.
- [6] H. Zhong, H. Zhang, G. Liu, Y. Liang, J. Hu, B. Yi, *Electrochem. Commun.* 8 (2006) 707–712.
- [7] D. Xia, S. Liu, Z. Wang, G. Chen, L. Zhang, L. Zhang, S.R. Hui, J. Zhang, *J. Power Sources* 177 (2008) 296–302.
- [8] Y. Feng, T. He, N. Alonso-Vante, *Chem. Mater.* 20 (2007) 26–28.
- [9] D. Susac, L. Zhu, M. Teo, A. Sode, K. Wong, P. Wong, R. Parsons, D. Bizzotto, K. Mitchell, S. Campbell, *J. Phys. Chem. C* 111 (2007) 18715–18723.
- [10] Y. Feng, T. He, N. Alonso-Vante, *Electrochim. Acta* 54 (2009) 5252–5256.
- [11] R. Liu, C. von Malotki, L. Arnold, N. Koshino, H. Higashimura, M. Baumgarten, K. Müllen, *J. Am. Chem. Soc.* 133 (2011) 10372–10375.
- [12] G. Sun, J. Wang, R. Savinell, *J. Appl. Electrochem.* 28 (1998) 1087–1093.
- [13] M. Lefevre, J.-P. Dodelet, *Electrochim. Acta* 48 (2003) 2749–2760.
- [14] R. Bashyam, P. Zelenay, *Nature* 443 (2006) 63–66.
- [15] K. Lee, L. Zhang, H. Lui, R. Hui, Z. Shi, J. Zhang, *Electrochim. Acta* 54 (2009) 4704–4711.
- [16] X. Yuan, X. Zeng, H.-J. Zhang, Z.-F. Ma, C.-Y. Wang, *J. Am. Chem. Soc.* 132 (2010) 1754–1755.
- [17] G. Wu, K.L. More, C.M. Johnston, P. Zelenay, *Science* 332 (2011) 443–447.
- [18] L. Yang, S. Jiang, Y. Zhao, L. Zhu, S. Chen, X. Wang, Q. Wu, J. Ma, Y. Ma, Z. Hu, *Angew. Chem.* 123 (2011) 7270–7273.
- [19] Z. Yang, Z. Yao, G. Li, G. Fang, H. Nie, Z. Liu, X. Zhou, X.a. Chen, S. Huang, *ACS Nano* 6 (2011) 205–211.
- [20] K. Gong, F. Du, Z. Xia, M. Durstock, L. Dai, *Science* 323 (2009) 760–764.
- [21] Y. Tang, B.L. Allen, D.R. Kauffman, A. Star, *J. Am. Chem. Soc.* 131 (2009) 13200–13201.
- [22] Z. Chen, D. Higgins, H. Tao, R.S. Hsu, Z. Chen, *J. Phys. Chem. C* 113 (2009) 21008–21013.
- [23] L. Qu, Y. Liu, J.-B. Baek, L. Dai, *ACS Nano* 4 (2010) 1321–1326.
- [24] S. Maldonado, K.J. Stevenson, *J. Phys. Chem. B* 109 (2005) 4707–4716.
- [25] M. Lefevre, J. Dodelet, P. Bertrand, *J. Phys. Chem. B* 104 (2000) 11238–11247.
- [26] M. Lefevre, J. Dodelet, P. Bertrand, *J. Phys. Chem. B* 106 (2002) 8705–8713.
- [27] M. Lefevre, J. Dodelet, P. Bertrand, *J. Phys. Chem. B* 109 (2005) 16718–16724.
- [28] M. Ferrandon, A.J. Kropf, D.J. Myers, K. Artyushkova, U. Kramm, P. Bogdanoff, G. Wu, C.M. Johnston, P. Zelenay, *J. Phys. Chem. C* 116 (2012) 16001–16013.
- [29] M. Bron, J. Radnik, M. Fieber-Erdmann, P. Bogdanoff, S. Fiechter, *J. Electroanal. Chem.* 535 (2002) 113–119.
- [30] G. Wu, C.M. Johnston, N.H. Mack, K. Artyushkova, M. Ferrandon, M. Nelson, J.S. Lezama-Pacheco, S.D. Conradson, K.L. More, D.J. Myers, *J. Mater. Chem.* 21 (2011) 11392–11405.
- [31] H.Y. Qin, Z.X. Liu, L.Q. Ye, J.K. Zhu, Z.P. Li, *J. Power Sources* 192 (2009) 385–390.
- [32] Y. Li, W. Zhou, H. Wang, L. Xie, Y. Liang, F. Wei, J.-C. Idrobo, S.J. Pennycook, H. Dai, *Nat. Nanotechnol.* 7 (2012) 394–400.
- [33] G. Liu, X. Li, P. Ganesh, B.N. Popov, *Electrochim. Acta* 55 (2010) 2853–2858.
- [34] S. Maldonado, K.J. Stevenson, *J. Phys. Chem. B* 108 (2004) 11375–11383.
- [35] P.H. Matter, L. Zhang, U.S. Ozkan, *J. Catal.* 239 (2006) 83–96.
- [36] H. Niwa, K. Horiba, Y. Harada, M. Oshima, T. Ikeda, K. Terakura, J.-i. Ozaki, S. Miyata, *J. Power Sources* 187 (2009) 93–97.
- [37] E.J. Biddinger, U.S. Ozkan, *J. Phys. Chem. C* 114 (2010) 15306–15314.
- [38] E.J. Biddinger, D. von Deak, U.S. Ozkan, *Top. Catal.* 52 (2009) 1566–1574.
- [39] S. Maldonado, S. Morin, K.J. Stevenson, *Carbon* 44 (2006) 1429–1437.
- [40] L. Lai, J. Potts, D. Zhan, L. Wang, C.K. Poh, C. Tang, H. Gong, Z. Shen, J. Lin, R. Ruoff, *Energy Environ. Sci.* 5 (2012) 7936–7942.
- [41] N.P. Subramanian, X. Li, V. Nallathambi, S.P. Kumaraguru, H. Colon-Mercado, G. Wu, J.-W. Lee, B.N. Popov, *J. Power Sources* 188 (2009) 38–44.
- [42] V. Nallathambi, J.-W. Lee, S.P. Kumaraguru, G. Wu, B.N. Popov, *J. Power Sources* 183 (2008) 34–42.
- [43] Z. Luo, S. Lim, Z. Tian, J. Shang, L. Lai, B. MacDonald, C. Fu, Z. Shen, T. Yu, J. Lin, *J. Mater. Chem.* 21 (2011) 8038–8044.
- [44] S. Ni, Z. Li, J. Yang, *Nanoscale* 4 (2012) 1184–1189.
- [45] T. Ikeda, M. Boero, S.-F. Huang, K. Terakura, M. Oshima, J.-i. Ozaki, *J. Phys. Chem. C* 112 (2008) 14706–14709.
- [46] H. Jin, H. Zhang, H. Zhong, J. Zhang, *Energy Environ. Sci.* 4 (2011) 3389–3394.
- [47] S. Liu, H. Zhang, Z. Xu, H. Zhong, H. Jin, *Int. J. Hydrogen Energy* 37 (2012) 19065–19072.
- [48] M. Lefèvre, E. Proietti, F. Jaouen, J.-P. Dodelet, *Science* 324 (2009) 71–74.
- [49] L. Zhang, K. Lee, C.W. Bezerra, J. Zhang, J. Zhang, *Electrochim. Acta* 54 (2009) 6631–6636.
- [50] H. Xiao, Z.-G. Shao, G. Zhang, Y. Gao, W. Lu, B. Yi, *Carbon* 57 (2013) 443–451.
- [51] T. Lopes, P. Olivi, *Electrocatalysis*, DOI 10.1007/s12678-014-0208-z.
- [52] D. Ohms, S. Herzog, R. Franke, V. Neumann, K. Wiesener, S. Gamburcev, A. Kaisheva, I. Iliev, *J. Power Sources* 38 (1992) 327–334.
- [53] C.H. Choi, S.H. Park, S.I. Woo, *Appl. Catal. B Environ.* 119 (2012) 123–131.
- [54] R. Pierotti, J. Rouquerol, *Pure Appl. Chem.* 57 (1985) 603–619.
- [55] M. Thommes, *Chem. Ing. Tech.* 82 (2010) 1059–1073.
- [56] E. Belyarova, K. Kaneko, *Adv. Mater.* 12 (2000) 1625–1628.
- [57] S.M.J.H. Kaufman, *Phys. Rev. B* 39 (1989) 13053–13060.
- [58] D. Saperstein, S. Metin, J. Kaufman, *Astrophys. J.* 342 (1989) L47–L50.
- [59] H.J. Zhang, H.C. Kong, X. Yuan, Q.Z. Jiang, J. Yang, Z.F. Ma, *Int. J. Hydrogen Energy* 37 (2012) 13219–13226.
- [60] F. Jaouen, M. Lefèvre, J.-P. Dodelet, M. Cai, *J. Phys. Chem. B* 110 (2006) 5553–5558.
- [61] G. Wu, M. Nelson, S. Ma, H. Meng, G. Cui, P.K. Shen, *Carbon* 49 (2011) 3972–3982.
- [62] Q. Li, P. Xu, W. Gao, S. Ma, G. Zhang, R. Cao, J. Cho, H.L. Wang, G. Wu, *Adv. Mater.* 26 (2014) 1378–1386.
- [63] U.I. Kramm, M. Lefèvre, N. Laroche, D. Schmeisser, J.P. Dodelet, *J. Am. Chem. Soc.* (2014). 10.1021/ja410076f.
- [64] J. Liu, X. Sun, P. Song, Y. Zhang, W. Xing, W. Xu, *Adv. Mater.* 25 (2013) 6879–6883.
- [65] D. Geng, Y. Chen, Y. Chen, Y. Li, R. Li, X. Sun, S. Ye, S. Knights, *Energy Environ. Sci.* 4 (2011) 760–764.
- [66] L. Zhang, Z. Xia, *J. Phys. Chem. C* 115 (2011) 11170–11176.
- [67] U.I. Koslowski, I. Abs-Wurmback, S. Fiechter, P. Bogdanoff, *J. Am. Chem. Soc.* 112 (2008) 15356–15366.